Cools *et al.*
EJNMMI Radiopharmacy and Chemistry (2025) 10:62
https://doi.org/10.1186/s41181-025-00386-z

EJNMMI Radiopharmacy and Chemistry

RESEARCH ARTICLE Open Access

[^{11}C]HSP990 PET as a translational tool to investigate the role of Hsp90 in tumours and support the development of Hsp90 therapeutics

Romy Cools[1†], Valeria Narykina[1,2,3†], Koen Vermeulen[4], Sanket J. Mishra[5], Brian S. J. Blagg[5,6], Marleen Derweduwe[7,8,9], Frederik De Smet[7,8,9], Aaron Ziani-Zeryouh[10], Matteo Riva[10,11], An Coosemans[10], Frederic Rousseau[2,3], Joost Schymkowitz[2,3] and Guy Bormans[1*]

†Romy Cools and Valeria Narykina are Joint first author.

*Correspondence: guy.bormans@kuleuven.be

[1] Present Address: Laboratory for Radiopharmaceutical Research, Department of Pharmaceutical and Pharmacological Sciences, KU Leuven, 3000 Louvain, Belgium
Full list of author information is available at the end of the article

Abstract

Background: Hsp90 is a molecular chaperone that is often overexpressed across multiple cancer types and has a potential value as a prognostic marker as well as a therapeutic target. Given the high interest in Hsp90 therapies, positron emission tomography or PET imaging of Hsp90 can be a valuable tool for patient selection. The limitations of the previously developed Hsp90 tracers prompted us to evaluate the recently developed brain-permeable [^{11}C]HSP990 PET probe to advance the development of Hsp90-targeted therapeutics. Given the brain accumulation of [^{11}C]HSP990 probe, application for glioblastoma imaging of this tracer is of particular interest.

Results: In vitro [^{11}C]HSP990 binding was assessed in breast cancer and glioma cell lines including patient-derived cells using Hsp90 inhibitors and RNA interference knockdown of Hsp90 isoforms. Saturation binding studies were conducted on these cells and tumour tissue homogenates, and autoradiography was performed on tissue sections. Ex vivo biodistribution and in vivo dynamic µPET/CT studies were performed in healthy mice and tumour-bearing mice, including immunocompromised subcutaneous human U87 and MDA-MB-231models and immunocompetent intracranial murine NS/CT-2A models at baseline and following a pre-treatment with Hsp90 inhibitors. High Hsp90-specific tracer uptake was observed in breast cancer and glioma cells, with Hsp90β inhibition resulting in the most substantial reduction in uptake. In vivo uptake was high in U87 tumours but low in MDA-MB-231, presumably due to the differences in Hsp90 expression in tumour tissue *versus* cultured cells. Differences in maximum binding capacity or B_{max} across cell and tissue types support this hypothesis, especially given that the affinity measured as dissociation constant K_d remained similar across all tissue types. Despite high NS/CT-2A tumour uptake in vitro, no contrast between the healthy brain tissue and the NS/CT-2A glioma was observed in vivo due to the high uptake by the healthy brain.

Conclusion: [^{11}C]HSP990 is a promising tracer for identifying Hsp90-overexpressing tumours and may hold potential for patient stratification, prognosis, and therapy

monitoring of novel Hsp90 therapeutics. High healthy brain uptake of this tracer precluded the differentiation of the tumour in the intracranial NS/CT-2A tumour model, therefore [^{11}C]HSP990 might not be a suitable tracer for the glioblastoma imaging. Tracer with a longer half-life might be needed to compare the washout of the tracer from the brain and the tumour tissue over several hours to identify a suitable imaging window.

Keywords: Cancer, Diagnostics, Glioblastoma, Heat shock proteins

Background

Heat shock protein 90 (Hsp90) belongs to a family of molecular chaperones consisting of small Hsps, Hsp40, Hsp60, Hsp70 and Hsp110, which were named after their corresponding molecular weight (MW). Hsps were first discovered as responders to heat stress upon which their cellular levels increase considerably, although their presence is also essential for the function of healthy cells under normal conditions. The primary role of Hsp90 along with its co-chaperones is to maintain proteostasis through assisting in protein folding, disaggregation and directing misfolded proteins towards degradation. Structurally, Hsp90 is a homodimer consisting of three domains: N-terminal domain (NTD) containing an adenosine triphosphate (ATP) binding site, the middle domain for protein–protein interactions, and the C-terminal dimerization domain joining two Hsp90 monomers. Hsp90 is an ATPase that hydrolyses ATP to adenosine diphosphate (ADP) and cycles through open (ATP-bound) and closed (ADP-bound) states, with ATPase activity required for its chaperoning function.

In humans and many other eukaryotes, four paralogues of Hsp90 exist: cytosolic Hsp90α and Hsp90β, glucose-regulated protein 94 (GRP94) in the endoplasmic reticulum, and tumour necrosis factor receptor associated protein 1 (TRAP1) in the mitochondria (Csermely et al. 1998). Hsp90 is essential and certain threshold levels in the cytosol are required for survival. Complete knockout (KO) of Hsp90α in mice is tolerated but results in male sterility, whereas full KO of Hsp90β is embryonically lethal and at least one allele of Hsp90β required for survival (Bhattacharya et al. 2022; Grad et al. 2010; Voss et al. 2000). While Hsp90 is present in most cells, exposure to stress triggers a heat shock response (HSR) leading to the increased expression of chaperones required for cell survival under stress. Heat shock factor protein 1 (HSF1) is a transcription factor responsible for the upregulation of Hsp90α in response to stress. While Hsp90α upregulation is mainly associated with the stress response, Hsp90β levels can also be upregulated via the internal ribosome entry site (IRES) such as in the case of single Hsp90β allele deletion (Bhattacharya et al. 2022).

Cancer cells learned to overexpress Hsp90 in order to survive hypoxia, starvation, oxidative and DNA damage. Given its vast interaction network, Hsp90 stabilizes oncoproteins such as HER2, c-MET, and mutant p53, aiding in cancer cell survival. The dependency of multiple oncoproteins on Hsp90 function makes it an attractive pan-cancer target. Elevated levels of Hsp90α determined by immunohistochemistry correspond with high [^{18}F]FDG uptake and poor prognosis in colorectal cancer (Nam and Lee 2021). High Hsp90 levels are found in the serum of some cancer patients and correlate with the disease progression in breast cancer (Liu et al. 2021a). Hsp90's role in glioblastoma

has been reviewed in detail by Babi et. al. (Babi et al. 2022). Elevated levels of Hsp90 in human glioma *versus* normal brain tissue were observed in biopsies (Canella et al. 2017). High Hsp90 expression levels can correlate with both good and poor survival prognosis dependent on the cancer type (Sartori et al. 2017). Hsp90 inhibitors were previously evaluated in glioblastoma models both as standalone treatments or in combination with other chemotherapies as well as tested as radiosensitizers and have demonstrated therapeutic effect in this aggressive tumour type (Canella et al. 2017; Orth et al. 2021). Non-invasive assessment of local Hsp90 status in malignancies using PET imaging in addition to the determination of serum Hsp90 levels could be beneficial to patient stratification, prognosis, as well as selection for Hsp90-targeting therapies and treatment follow up in glioblastoma and other cancers.

Most small molecule Hsp90 inhibitors developed to date target the ATP-binding pocket and block its chaperone activity leading to the client degradation, although inhibitors targeting other epitopes on Hsp90 have also been reported and comprehensively reviewed (Rastogi et al. 2024). N-terminal domain inhibitors of Hsp90 are known to induce HSR leading to the upregulation of Hsp70 and other heat shock proteins in response to the treatment, which is thought to be one of the main reasons behind the limited success of the pan-Hsp90 treatments in the clinic (Rastogi et al. 2024). The first Hsp90α/β isoform-specific inhibitor Pimitespib (TAS-116, Jeselhy®) that does not trigger a HSR was recently registered in Japan for the treatment of gastrointestinal stromal tumours, breaking the stalemate of slow clinical progress experienced with other inhibitors (Kurokawa et al. 2022). Group of Dr. Blagg developed Hsp90β-selective inhibitors that exhibited cytotoxicity in tumour cells without inducing the HSR, hence circumventing resistance mechanisms observed with some other pan-Hsp90 inhibitors in the clinical trials and offering promise as therapeutic candidates.

Treatment response to the Hsp90-targeting therapies has been monitored using tracers targeting tumour metabolism and proliferation with [^{18}F]FDG and [^{18}F]FLT in breast tumour and glioblastoma models (Monazzam et al. 2009); [^{68}Ga]Ga-DOTA-F(ab9)2-herceptin and [^{89}Zr]Zr-trastuzumab in breast and ovarian cancers expressing HER2 (Oude Munnink et al. 2010; Smith-Jones et al. 2006); and c-MET expression with [^{89}Zr]Zr-onartuzumab, amongst others (Pool et al. 2017). However, there is no approved and routinely used Hsp90 radiotracer for the evaluation of Hsp90 status in cancer patients. Hsp90-specific tracer can support the design of novel Hsp90 inhibitors and shed light on the limited success seen with the Hsp90 inhibitors in the clinical trials. We and others explored Hsp90 imaging directly with radiolabelled Hsp90 inhibitors in the in vitro and in vivo tumour models. Previous tracers based on 4-(N-(S-glutathionylacetyl)amino) phenylarsonous acid (GSAO), namely [^{111}In]In-DTPA-GSAO and [^{67}Ga]Ga-DOTA-GSAO, targeted cytosolic Hsp90 released by dead cells after membrane rupture (Ho Shon et al. 2020; Park et al. 2011). Series of peptide radiotracers based on the Sansalvamide A-amide inhibitor including [^{18}F]F-PEGylated San A visualized pancreatic cancer in PL45 xenograft model (Wang et al. 2024; Wang et al. 2022; Wang et al. 2018). [^{124}I]PU-H71 and [^{124}I]PU-AD have shown tumour accumulation and progressed to clinical trials, however high gastrointestinal uptake limits its applicability for routine use (Bolaender et al. 2021a; Dunphy et al. 2020). [^{18}F]PTP-Ganetespib showed blockable uptake in vitro, but low tumour accumulation in vivo and high background (Kang et al.

2018). Luminespib-derivative [^{18}F]9 showed specific binding in pancreatic neuroendocrine tumour models in vitro, which did not translate in vivo due to too rapid plasma clearance (Nordeman et al. 2021). Geldanamycin-based [^{64}Cu]Cu-DOTA-BDA-GM demonstrated tumour uptake in vivo and detection of metastatic breast cancer, where longer half-life of copper-64 enabled better contrast at 18 h post-injection (*p.i.*) (Li et al. 2024). The most recent tracer, [^{11}C]BIIB021, was evaluated for brain imaging, but has not been studied for cancer imaging (Sakai et al. 2024). We previously reported multiple Hsp90 tracers for tumour imaging: [^{11}C]NMS-E973 and [^{11}C]YC-72-AB85 which exhibited blockable uptake in vitro and in vivo across multiple tumour types but had low (< 1.0) tumour standardized uptake values (SUVs), [^{11}C]SNX-ab which targeted tumour in vitro but was abandoned due to the incomplete specificity towards Hsp90 (Cools et al. 2023; Vermeulen et al. 2021; Vermeulen et al. 2019), as well as [^{18}F]FEHSP990 which lost its binding affinity towards Hsp90 compared to the original [^{11}C]HSP990 radiotracer developed for brain imaging. Given the current state of Hsp90 PET tracers, there is a need for a better candidate with selectivity towards Hsp90, better tumour uptake and retention, and more favourable pharmacokinetics with minimal uptake in non-target organs. This study aims to evaluate [^{11}C]HSP990 brain probe for cancer PET imaging with a particular interest in glioblastoma imaging given the known blood–brain barrier (BBB) permeability of this tracer.

Methods

Reagents and chemicals

Synthesis of the precursor compound, (*R*)-2-amino-7-(4-fluoro-2-(6-hydroxypyridin-2-yl)phenyl)-4-methyl-7,8-dihydropyrido[4,3-*d*]pyrimidin-5(6*H*)-one, was performed as previously described (unpublished data). SNX-0723 ((S)-2-fluoro-6-((tetrahydrofuran-3-yl)amino)-4-(3,6,6-trimethyl-4-oxo-4,5,6,7-tetrahydro-1H-indol-1-yl)benzamide) was synthesized as previously reported (Huang et al. 2009). The reference compound HSP990, (*R*)-2-amino-7-(4-fluoro-2-(6-methoxypyridin-2-yl)phenyl)-4-methyl-7,8-dihydropyrido[4,3-*d*]pyrimidin-5(6*H*)-one, other Hsp90 inhibitors, including Onalespib, PU-H71, PU-WS13 and TAS-116, and HDAC6 inhibitor ACY-775 were purchased from commercial suppliers (Biorbyt, Selleckchem Chemicals, MedChem Express or CSNpharm), analyzed by liquid chromatography-mass spectrometry (LC–MS) and/or nuclear magnetic resonance (NMR) to confirm their identity and used without further purification. Isoform-selective Hsp90 inhibitors were kindly provided by prof. Brian Blagg. Chemical structures were drawn using ChemDraw Ultra 15.0 (Perkin Elmer). An overview of all Hsp90 inhibitors used in this study, along with their corresponding MWs and reported affinity profiles, is provided in Supplementary Table 1.

LC–MS

Intermediate reaction products were characterized using a Dionex Ultimate 3000 LC system (Thermo Fisher Scientific, Sunnyvale, USA) coupled to a high-resolution time-of-flight mass spectrometer (MaXis Impact, Bruker, Bremen, Germany) equipped with an orthogonal electrospray interface. Acquisition and processing of data were performed using Compass IsotopePattern (version 3.2, Bruker).

High-performance liquid chromatography (HPLC) analysis

HPLC was performed on a LaChrom Elite HPLC system (Hitachi, Darmstadt, Germany) connected to a Waters 2487 UV–VIS detector and a 3-inch NaI(Tl) scintillation detector connected to a single channel analyzer (Gabi, Raytest, Straubenhardt, Germany). Registration and integration of the HPLC chromatograms was performed with GINA Star (Raytest) software.

Cell lines and cell culture

MDA-MB-231 and U87 cell lines were obtained from American Type Culture Collection (ATCC) and grown in Dulbecco's Modified Eagle's Medium (DMEM, high glucose, Gibco, 41,965–039, Thermo Fisher Scientific) supplemented with 10% fetal bovine serum (FBS), 1X MEM non-essential amino acids (Gibco, 11,140–035, Thermo Fisher Scientific) and 1 mM Sodium Pyruvate (Gibco, 11,360–039, Thermo Fisher Scientific). Cells were kept in the humidified chamber at 37 °C and 5% CO_2 and subcultured using using TrypLE™ Select Enzyme (1X), no phenol red, (Gibco, 12,563,029, Thermo Fisher Scientific). Cell passage was kept under 20 for all experiments performed in this study. All cells were kept free of mycoplasma contamination throughout all studies.

CT-2A cells were kindly provided by Prof. Thomas Seyfried (Boston College, Boston, MA) and were incubated at 37 °C in humidified air with 5% CO_2 (Seyfried et al. 1992). CT-2A neurospheres (NS/CT-2A) were generated via serum-free culture in DMEM/Nutrient Mixture F-12 (DMEM/F-12, Sigma-Aldrich) supplemented with 20 ng/mL of epidermal growth factor (EGF, Thermo Fisher Scientific), 20 ng/mL of fibroblast growth factor (FGF, Thermo Fisher Scientific), 2 µg/mL Heparin and 2% B27 supplement (Thermo Fisher Scientific).

Patient-derived cell lines (PDCLs), LBT005 and CME038, were obtained from the Laboratory for Precision Cancer Medicine at KU Leuven. These PDCLs were established from fresh tumor tissue collected from patients undergoing surgical resection at UZ Gasthuisberg (all patients provided informed consent) or from retrospective dissociated tumor tissue samples obtained from the Center for Human Genetics. The Ethics committee approved the use of these established PDCLs under protocol S69409. PDCLs were cultured in NeuroCult™ NS-A Basal Medium (Human), supplemented with NeuroCult™ NS-A Proliferation Supplements (STEMCELL Technologies, #05751), heparin solution (2 mg/mL, STEMCELL Technologies, #07980), human recombinant basic fibroblast growth factor (bFGF, 20 ng/mL, STEMCELL Technologies, #78,003.2), human recombinant epidermal growth factor (EGF, 20 ng/mL, STEMCELL Technologies, #78,006.2), and Antibiotic–Antimycotic (100X, 5 mL, Gibco™, #15,240,062). Cultures were maintained in flasks pre-coated with laminin (Sigma, #L2020). Cell cultures were incubated in a humidified atmosphere at 37 °C with 5% CO_2. The culture medium was replenished twice weekly, and cells were passaged upon reaching approximately 80% confluence.

Hsp90 isoform knockdown in U87 and MDA-MB-231 cell lines

Dicer substrate small interfering RNA (DsiRNA) knockdown (KD) protocol was adapted from our previous work (Narykina et al. 2025). For cell binding experiments with [^{11}C] HSP990, 125,000 cells/well were seeded in 6-well plates. Hsp90 DsiRNA KD experiment

was performed as follows: 10 nmol DsiRNA targeting Hsp90α (DsiRNA 13.1, IDT) and Hsp90β (DsiRNA 13.2, IDT), or negative control DsiRNA (IDT) were formulated in 0.5 mL Opti-MEM™ I Reduced Serum Medium, no phenol red (Gibco™) and added to the wells, followed by addition of 5 µL Lipofectamine™ RNAiMAX Transfection Reagent (Invitrogen™). The reagents were allowed to equilibrate for 20–30 min after which 2 mL of regular cell media containing the appropriate number of cells was added to the wells and incubated for 48 h in the humidified chamber at 37 °C and 5% CO_2. KD was verified by assessing Hsp90 protein levels using western blot (WB). Total protein amount in the cell lysates was determined by BCA Rapid Gold assay (Thermo Fisher Scientific). The amount of each Hsp90 isoform in cell lysates was determined by standard curve with recombinant Hsp90α (produced in house) and Hsp90β (ab80033, Abcam). The % KD was determined by normalizing signal to GAPDH and negative control lysate: %KD = (Hsp90 KD signal / GAPDH KD signal) / (Hsp90 NC signal / GAPDH NC signal) × 100%. The amount of Hsp90 isoforms in each tissue type was calculated from a WB standard curve in GraphPad Prism 10.0 software and expressed as %total by dividing the calculated protein amounts by 6 µg that was loaded on the gel. The amounts are expressed as average (n = 3) ± standard deviation (SD).

For cell binding experiments with [^{3}H]HSP990, 8,000–15,000 cells/well were seeded in 96-well plates. Both DsiRNAs (10 nmol) and Lipofectamine (0.2 µL/well) were pre-formulated in transfection media, 10 µL of each reagent was added to the wells and allowed to equilibrate for 20–30 min. Appropriate number of cells was added in the 100 µL of regular cell media on top of the DsiRNA transfection reagents and incubated for 48 h in the humidified chamber at 37 °C and 5% CO_2. KD was verified by assessing Hsp90 protein levels using immunofluorescence (Narykina et al. 2025).

Protein quantification by WB

General procedure was followed (Narykina et al. 2025). Per each lane, 6 µg of cell lysates protein or 3 µg of tissue protein and varying amounts of recombinant protein (6.25ng—0.1 µg) were loaded on the gel (any KD™ Mini-PROTEAN® TGX™ Precast Protein Gels, BioRad). Protein was then transferred to the nitrocellulose membrane (Trans-Blot Turbo Mini, BioRad), and membrane was blocked in 5% BSA in TBS-T for 1 h. Primary antibody incubation was performed overnight at 4 °C (1:1000 anti-Hsp90α, 68/Hsp90 Abcam; 1:1000 anti-Hsp90β, E296 Abcam). Membranes were washed in TBS-T buffer 3 × 10 min and incubated with 1:10,000 Rhodamine Anti-GAPDH and 1:2500 StarBright700 secondary antibodies (BioRad) in blocking buffer for 1 h, washed and imaged using ChemiDoc™ MP Imaging System (BioRad). Image analysis was performed in Image Lab software (BioRad). Standard curve was used to determine the amount of Hsp90 protein in samples of interest.

Half maximal inhibitory concentration (IC_{50}) assays

LBT005 and CME038 cells were dissociated into single cells using Accutase Stempro (Gibco, #A1110501) and counted with a Bio-Rad TC20™ cell counter. The cells were seeded at a density of 10,000 cells per well in the laminin-coated 96-well plate and incubated for 24 h (5% CO_2, 37°, 100% humidity). NS/CT-2A cells were seeded at a density of 10,000 cells per well in the 110 µL of cell culture medium in the 96-well flat-bottom

plates. All cells were treated with Hsp90 inhibitors, starting at a concentration of 10 µM, and subjected to a 1:3 serial dilution. The final dimethylsulfoxide (DMSO) concentration was maintained at 0.1%. Treated cells were incubated for 72 h (5% CO_2, 37°, 100% humidity). Cell viability was assessed using the CellTiter-Glo® Luminescent Cell Viability Assay (Promega, #G7573), which measures ATP levels as an indicator of metabolically active cells. After the addition of 100 µL of CellTiter-Glo® reagent per well, the NS/CT-2A cell suspensions were transferred to opaque-walled plates (Greiner Lumitrac, ref: 655,074). The luminescence readout was performed using a SpectraMax i3 plate reader. Data analysis was conducted using GraphPad Prism 10 software.

Animals

All mice were kept in a thermoregulated (22 °C) and humidity-controlled environment with a 12/12 h light/dark cycle in individual ventilated cages and had free access to food and water. All animal experiments were conducted after approval of the local University Ethics Committee for Animals (P190-2019 and P169-2024) and carried out in accordance with the ARRIVE guidelines. Female CB17.Cg-Prkdc < scid > Lyst < bg-J > /Crl (SCID/beige) mice, 5–6 weeks old (body weight 20–25 g), were purchased from Charles River Laboratories (Sulzfeld, Germany). Female C57BL/6J mice, 10–15 weeks old (body weight 20–25 g), were obtained from Janvier (La Genest-Saint Isle, France). Female animals were chosen as they are generally more docile in nature. Animals were allowed to acclimatize for at least one week before start of the experiments.

Generation of tumor models

Mice were anesthetized with 2.5% isoflurane in O_2 at a flow rate of 1 L/min. A total of 1×10^6 U87 or MDA-MB-231 cells mixed with Cultrex (1:1; Cultrex Basement Membrane Extract, R&D systems, Minneapolis, MN, USA) to a total volume of 100 µL per mouse, were subcutaneously inoculated into the right shoulder of female 10-week-old SCID mice. The tumors were allowed to grow for 4–8 weeks until they reached 50–75 mm^3 or 150–200 mm^3 in size (measured by caliper, h×l×w), after which the animals were used for ex vivo biodistribution and in vivo imaging studies.

NS/CT-2A derived cells were intracranially injected into C57BL/6J mice as previously described (Riva et al. 2019). Briefly, mice were anesthetized via intraperitoneal (IP) injection of 6 µL/g body weight of a mixture containing 18.75 mg/mL ketamine (Pfizer) and 0.125% xylazine (Bayer). After enzymatical dissociation (Stempro Accutase, Thermo Fisher Scientific), a total of 5×10^4 NS/CT-2A cells suspended in 2 µL of DMEM/F-12 were inoculated 2.5 mm lateral from the midline, 0.5 mm anterior to the bregma, and 2.5 mm below the dura mater using a 5 µL Hamilton syringe (Hamilton, #88,000) in a stereotactic frame (Stoelting). The stereotactic inoculation was performed under sterile conditions.

Mice tissue homogenate samples preparation

Mice were anesthetized with 2.5% isoflurane in O_2 at a flow rate of 1 L/min after which they were sacrificed by decapitation. Tumor and muscle tissues were excised, rinsed with saline to remove blood and rapidly frozen in cooled 2-methylbutane (-40 °C). The frozen tumors were mechanically homogenized in ice-cold 50 mM tris(hydroxymethyl)

aminomethane hydrochloride (Tris HCl)/0.9% NaCl pH 7.4 using a Potter–Elvehjem Tissue Homogenizer (VWR) to a concentration of 100 mg/mL wet tissue weight. Homogenate samples were stored at − 20 °C and thawed at the day of the experiment. For WB sample preparation, homogenized tissues were aspirated with a 27G needle followed by sonication on ice (3 s on, 10 s off interval for 10 cycles, 50% amplitude), and lysates were cleared by centrifugation at 14,000 × g for 15 min at 4 °C.

Total protein amount in the tissue was determined by BCA Rapid Gold assay (Thermo Fisher Scientific). The amount of each Hsp90 isoform was determined by standard curve with recombinant Hsp90α (produced in house) and Hsp90β (ab80033, Abcam). The amount of Hsp90 isoforms in each tissue type was calculated from a WB standard curve in GraphPad Prism 10.0 software and expressed as %total by dividing the calculated amounts by 3 µg that was loaded on the gel. The amounts are expressed as average (n = 3) ± SD.

Tissue sections

Mice were anesthetized with 2.5% isoflurane in O_2 at a flow rate of 1 L/min after which they were sacrificed by decapitation. MDA-MB-231, U87, NS/CT-2A tumor tissue was excised, rinsed with saline to remove blood and rapidly frozen in cooled 2-methylbutane (-40 °C). Cryotome sectioning (Shandon cryotome FSE, Thermo Fisher Scientific, Waltham, MA) was performed to obtain 20 µm-sections, which were fixed on adhesive microscope slides (Superfrost Plus, Thermo Fisher Scientific) and stored at − 20 °C. PC3 and B16.F10 tumor tissue sections were obtained from previous studies (Vermeulen et al. 2019).

Immunofluorescent and histological staining of tumor tissue sections

Tissues were stained manually by first rinsing thawed tissues with TBS, blocking for 2 h at RT in blocking buffer (TBS, 0.3% Triton X-100, 0.3 M Glycine, 10% goat serum), followed by primary antibody incubation at 1:100 dilution (anti-Hsp90α, 68/Hsp90 Abcam; anti-Hsp90β, E296 Abcam) overnight at 4 °C in TBS buffer (TBS, 0.3% Triton X-100, 5% goat serum). Tissues stained with secondary only antibody were used as a control. Tissue slides were then rinsed with TBS × 3, incubated with AlexaFluor647-labeled secondary antibody for 1 h, rinsed with TBS × 3 followed by Milli-Q® water, mounted with ProLong™ Gold Antifade Mountant with DNA Stain DAPI (Invitrogen™) and imaged using a Zeiss Axio Scan.Z1 automated slide scanner. Images were prepared for publication using Zen and QuPath softwares.

Hematoxylin–eosin (H&E) staining was performed as follows: tissue sections were deparaffinized at 50 °C for 1 h, followed by sequential immersions in toluene (2 × 5 min) and ethanol (2 × 5 min). Slides were rehydrated using tap and distilled water. Hematoxylin Gill 3 (Prosan) was applied for 4 min, followed by rinsing. Acid alcohol (1% HCl in 100% ethanol) was used for differentiation with three dips, then slides were rinsed and neutralized with lithium carbonate (saturated in distilled water) until blue. After further rinsing, sections were stained with eosin (1%, Prosan) for 3 min. Final steps included one dip each in tap and distilled water, rapid dehydration through graded propanol and neoclear, and mounting with Neomount.

Radiosynthesis of [^{11}C]HSP990

The radiosynthesis was performed as previously described (Cools et al. 2025b). Briefly, [^{11}C]CH_4 was produced by proton irradiation of a N_2+H_2 (10%) gas mixture in a Cyclone 18/9 cyclotron (IBA Louvain-la-Neuve, Belgium) and converted to [^{11}C]CH_3I in a home-built gas phase recirculation module. [^{11}C]HSP990 was synthesized by O-methylation of the corresponding phenol HSP990 precursor (300–450 µg) by bubbling [^{11}C]CH_3I through a solution with Cs_2CO_3 (1.5–2.5 mg) dissolved in anhydrous dimethylformamide (DMF) (150–200 µL) at 120 °C for 3 min. The crude reaction mixture was purified by HPLC on a RP-C_{18} column (XBridge C18 column, 5 µm, 4.6 mm × 150 mm; Waters, Milford, USA) eluted with 30/70 V/V CH_3CN/HCO_2NH_4 0.05M 50 mM at a flow rate of 1.5 mL/min. The final product was formulated using a single use C_{18} Sep-Pak® solid phase extraction (SPE) cartridge in approximately 1.1 mL ethanol and 11.9 mL NaCl 0.9% solution in water for injection and filtered through a single-use sterile syringe filter (Millex-GV filter 0.22 µm, ø 13 mm Millipore, Billerica, MA) into a sterile vial. An aliquot (100 µL) was taken for quality control (QC) analysis by HPLC on a HSS PFP column (XSelect HSS PFP 3.5 µm, 4.6 × 150 mm) eluted with 43/57 V/V CH_3CN/0.1% HCOOH in H_2O at a flow rate of 1.0 mL/min to assess chemical and radiochemical purity. Molar activity of [^{11}C]HSP990 was 150 ± 50 GBq/µmol at the end of synthesis.

Quantification of radioactivity in biological samples

Quantification of [^{11}C]HSP990 radioactivity was performed with an automated gamma counter equipped with a 3-inch NaI(Tl) well crystal coupled to a multichannel analyzer (Wallac 1480 Wizard, Wallac, Turku, Finland). The results were corrected for background radiation, physical decay during counting and detector dead time.

In vitro [^{11}C]HSP990 cell binding assay

Cells were seeded at 100–125,000 cells/well density in 6-well plates and incubated at 37 °C for 48 h in the presence of 5% CO_2. DsiRNA KD of Hsp90 isoforms was performed as described (Narykina et al. 2025). Cells were gently washed once with PBS and pre-incubated with either vehicle (cell culture medium + 1% DMSO) as baseline control or 100 µM of HSP990, Onalespib, PU-H71, A1, A2, B1, B2, C1, C2, D3, PU-WS-13 or TAS-116 dissolved in vehicle for 60 min at 37 °C and 5% CO_2 (Fig. 1, Supplementary Table 1). Next, the pre-incubation solutions were removed, and the cells were gently washed once with PBS. The cells were subsequently incubated with 250 kBq/mL of [^{11}C]HSP990 dissolved in cell culture medium (total 1% ethanol) for 30 min at 37 °C. After incubation, cells were washed three times with 1 mL of ice-cold PBS and PBS wash fractions were collected. Cells were lysed by adding 400 µL of the lysis buffer (reagent A100, Chemometec, Allerod, Denmark) and gently mixing by pipetting. The lysis buffer was collected and quenched with 400 µL of the neutralization buffer (reagent B, Chemometec, Allerod, Denmark) by first washing the wells and then adding the neutralization buffer to the lysed fraction. The PBS wash and lysed fractions were counted for their radioactivity in an automated gamma counter as described above. Finally, the number of cells per well was counted using an automated counting device with nucleocasettes (NucleoCounter®

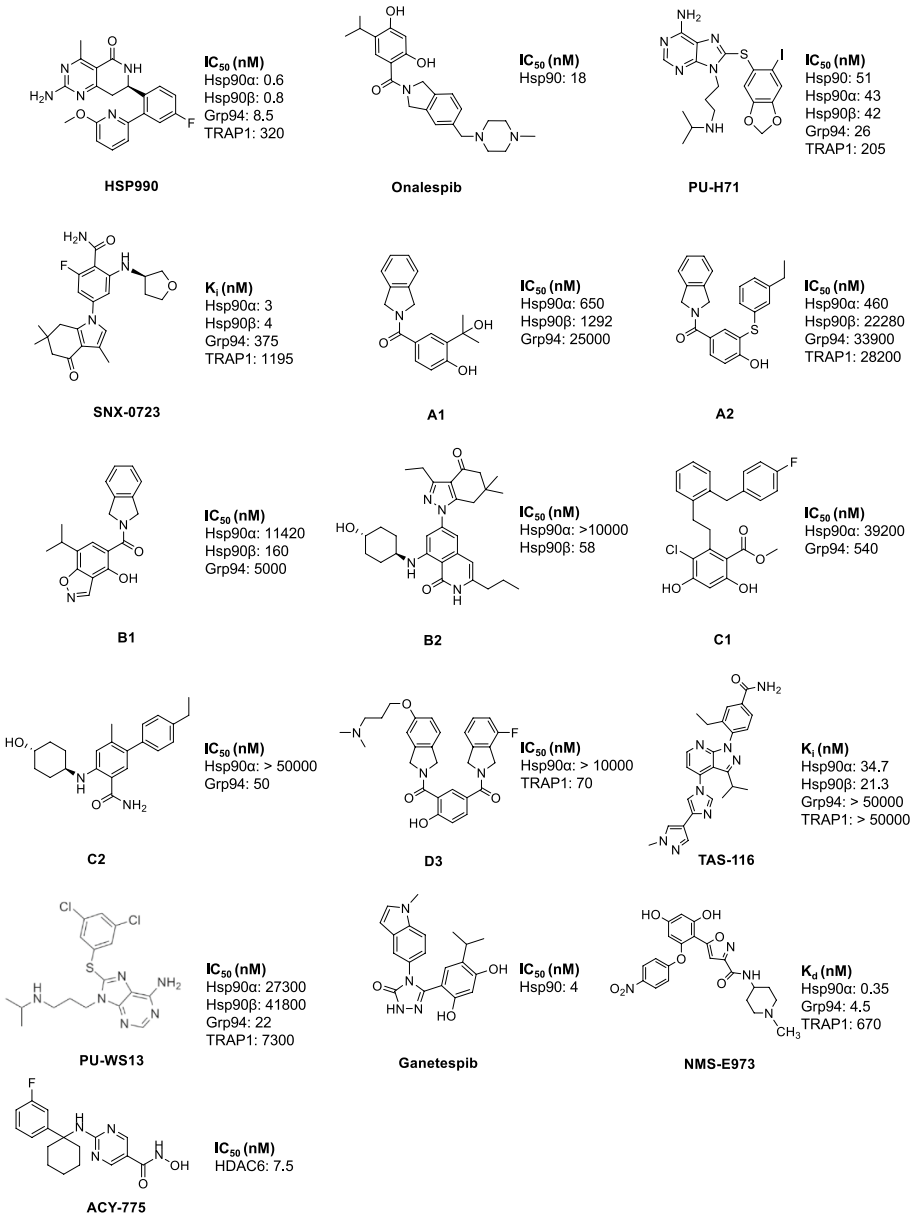

Fig. 1 Overview of all Hsp90 inhibitors used in this study. IC_{50} = half maximal inhibitory concentration, K_i = inhibition constant

NC-200™, Chemometec). Data were expressed as percentage of the applied radioactivity bound to 1×10^5 cells or as percentage of the applied radioactivity bound to 1×10^5 cells normalized to the baseline control conditions and presented using GraphPad Prism 10.0 software as mean ± SD, n = 3 wells per pre-incubation condition.

In vitro [^{3}H]HSP990 cell saturation binding

[^{3}H]HSP990 (38 MBq/mL, radiochemical purity > 99%, molar activity 3.07 TBq/mmol) was obtained from Novandi Chemistry AB. Cells were seeded at 8,000 cells/well density in 96-well plates and incubated at 37 °C for 48 h in the presence of 5% CO_2. DsiRNA KD of Hsp90 isoforms was performed as described (Narykina et al. 2025).Cells were gently

washed once with 50 mM Tris/0.9% NaCl pH 7.4 and incubated with increasing concentrations of 0.01 nM—60 nM of [^{3}H]HSP990 in cell medium in a final assay volume of 200 µL for 60 min at 37 °C. Co-incubation with 10 µM HSP990 was performed to determine non-specific binding (NSB). After incubation, incubation solutions were removed and cells were detached from the wells using TrypLE™ Select Enzyme (1X), no phenol red, (12,563,029, Gibco, Thermo Fisher Scientific) Next, cells (=bound tracer) were collected by filtration onto UniFilter-96 GF/C Microplates (Perkin Elmer) (presoaked in 0.3% polyethylenimine (PEI)) using a Perkin Elmer FilterMate Harvester Unifilter-96 and rapidly washed three times with ice-cold Tris/0.9% NaCl pH 7. The filter plates were collected and dried overnight. Next, 20 µL of Microscint-20 (Perkin Elmer) was added to each well of the filter plates and filter plates were counted using a Perkin Elmer TopCount (1 min counting time per well to determine counts per minute (CPM)). Data were expressed as bound tracer (calculated as total binding (TB)—NSB) in fmol per 10^5 cells versus incubated tracer concentration in nM. A non-linear regression one-site specific curve fit was applied using GraphPad Prism 10.0 software to calculate B_{max} (pmol/10^5 cells) and K_d (nM) values. Data were presented as mean ± SD, n = 3 wells per pre-incubation condition.

In vitro [^{3}H]HSP990 tissue homogenate saturation binding

Homogenate samples were diluted to achieve a final concentration of 5–10 µg of protein per well in a final assay volume of 200 µL and incubated with increasing concentrations of 0.01 nM—60 nM of [^{3}H]HSP990 in 50 mM Tris/0.9% NaCl pH 7.4 for 60 min at 37 °C. Co-incubation with 10 µM HSP990 was performed to determine NSB. After incubation, unbound and bound tracer were separated by filtration onto UniFilter-96 GF/C Microplates (Perkin Elmer) (presoaked in 0.3% PEI) using a Perkin Elmer FilterMate Harvester Unifilter-96 and rapidly washed three times with ice-cold Tris/0.9% NaCl pH 7. The filter plates were collected and dried overnight. Next, 20 µL of Microscint-20 (Perkin Elmer) was added to each well of the filter plates and filter plates were counted using a Perkin Elmer TopCount (1 min counting time per well to determine CPM). Data were expressed as bound tracer (calculated as total binding (TB)—NSB) in fmol per mg protein versus incubated tracer concentration in nM. A non-linear regression one-site specific curve fit was applied using GraphPad Prism 10.0 software to calculate B_{max} (pmol/mg) and K_d (nM) values. Using MW of Hsp90, B_{max} values were expressed as percentage of total protein concentration and the ratio of Hsp90α/β protein concentration determined by WB (%) to B_{max}(%) was determined. Data were presented as mean ± SD, n = 3 mice per xenograft type/3 samples per incubation condition.

In vitro [^{11}C]HSP990 autoradiography

Frozen tissue sections were air-dried and washed in Tris HCl buffer (50 mM, pH 7.4) for 10 min at room temperature. Sections were subsequently air-dried and pre-incubated with either vehicle (Tris HCl buffer + 0.3% BSA + 10% DMSO) as baseline control or 10 µM of HSP990, Onalespib, PU-H71 or SNX-0723 dissolved in vehicle for 10 min at room temperature. Next, the pre-incubation solutions were removed, and the sections were dipped in Tris HCl buffer + 0.3% BSA at 4 °C. The sections were again air-dried and subsequently incubated with 74 kBq/mL of [^{11}C]HSP990 dissolved in Tris HCl buffer + 0.3%

BSA for 10 min at room temperature. After incubation, the sections were washed twice for 5 min in Tris HCl buffer + 0.3% BSA at 4 °C with a final dip in water at 4 °C. The air-dried slices were exposed to a phosphor storage screen (super-resolution screen; Perkin Elmer, Waltham, MA) overnight. The autoradiograms were obtained by reading the screens using a Cyclone Plus system (Perkin Elmer). Autoradiography images were analyzed using Optiquant software (Perkin Elmer) and intensity was expressed as digital light units per square mm (DLU/mm^2). Percentage block versus control was calculated as (1—((average DLU/mm^2 in the presence of 100 μM blocker)) / (average DLU/mm^2 tracer only))) × 100% and data were presented as mean ± SD, n = 3–4 tissue sections per pre-incubation condition.

In vivo [^{11}C]HSP990 μPET/CT imaging

U87 tumor mice were imaged with [^{11}C]HSP990 PET 4–5 weeks after cell inoculation when the tumors were 150–200 mm^3 in size. NS/CT-2A tumor mice were imaged with [^{11}C]HSP990 PET at 2 weeks after cell inoculation. MDA-MB-231 tumor mice were imaged with 2-[^{18}F]fluoro-2-deoxy-D-glucose ([^{18}F]FDG) and [^{11}C]HSP990 PET at 4–5 weeks after cell inoculation when the tumors were 50–75 mm^3 in size, and with [^{11}C]HSP990 at 7–8 weeks after cell inoculation when the tumors were 150–200 mm^3 in size. For [^{18}F]FDG imaging, the mice were subjected to an overnight fasted state with only access to water. After the abstinence period, mice were anesthetized using 2.5% isoflurane in O_2 at a flow rate of 1 L/min and intravenously (*i.v.*) injected with ~ 4 MBq of [^{18}F]FDG via a tail vein. Mice were allowed to recover consciousness during the uptake period of [^{18}F]FDG and at 60 min. post [^{18}F]FDG injection they were anesthetized and scanned statically for 10 min using Molecubes (β-CUBE), followed by a CT scan using Molecubes (X-CUBE), allowing full body field of view (FOV) PET/CT imaging. For [^{11}C]HSP990 imaging, mice were anesthetized using 2.5% isoflurane in O_2 at a flow rate of 1 L/min and *i.v.* injected with ~ 4 MBq of [^{11}C]HSP990 via a tail vein and scanned dynamically for 90 min using Molecubes (β-CUBE), followed by a CT scan using Molecubes (X-CUBE), allowing full body field of view (FOV) PET/CT imaging. To assess Hsp90 binding specificity, mice were pre-treated by intraperitoneal (*i.p.*) injection 60 min before [^{11}C]HSP990 injection of either vehicle (aqueous solution of 10% DMSO and 90% (2-hydroxypropyl)-β-cyclodextrin (40%) in H_2O) as baseline control or HSP990 or Onalespib (5 mg/kg) dissolved in vehicle. Pretreatment solutions were sterile filtered through a 0.22 μm membrane filter (Millex-GV, Millipore). Dynamic PET data were histogrammed into 17 frames (4 × 15, 1 × 38, 3 × 60, 1 × 180, 1 × 450, 7 × 600 s) and reconstructed using 30 iterations of the manufacturer's MLEM algorithm with corrections for randoms, scatter, attenuation and decay into a 192 × 192 image matrix containing 0.4 mm voxels. CT data were reconstructed using a regularized statistical (iterative) image reconstruction algorithm using non-negative least squares, using an isotropic 200 μm voxel size and scaled to Hounsfield Units (HUs) after calibration against a standard air/water phantom. Analysis of the PET/CT images was performed using the PMOD version 3.2 software (PMOD Technologies Ltd., Zurich, Switzerland). A manual volume of interest (VOI) was drawn over the tumor after normalizing for injected dose and bodyweight to generate tumor time-activity curves (TACs) scaled to SUV. No corrections for the

plasma radiometabolites were performed for the input function. Data were presented using GraphPad Prism 10.0 software as mean ± SD, n = 3 per pre-treatment condition.

Ex vivo [^{11}C]HSP990 biodistribution

U87, MDA-MB-231 and NS/CT-2A tumor mice were studied for ex vivo biodistribution after in vivo PET/CT imaging. Mice were anesthetized using 2.5% isoflurane in O_2 at a flow rate of 1 L/min and *i.v.* injected with ~ 5 MBq of [^{11}C]HSP990 via a tail vein. To assess Hsp90 binding specificity, mice were pre-treated by *i.p.* injection 60 min before tracer injection of either vehicle (aqueous solution of 10% DMSO and 90% (2-hydroxypropyl)-β-cyclodextrin (40%) in H_2O) as baseline control or HSP990 or Onalespib (10 mg/kg) dissolved in vehicle. Pretreatment solutions were sterile filtered through a 0.22 µm membrane filter (Millex-GV, Millipore). The mice were subsequently sacrificed by decapitation at 60 min post tracer injection. All organs of interest, including blood, were collected in tared tubes and weighed. The radioactivity in each organ was counted in an automated gamma counter as described above. For the calculation of the total radioactivity in blood, muscle and bone, the masses were assumed to be respectively 7%, 40% and 12% of the total body mass (Burns et al. 2007; Horti et al. 2006; Vermeulen et al. 2019). An additional blood sample was taken from the collected blood into a heparinized capillary microhematocrit tube (Globe Scientific). Plasma, buffy coat and red blood cells were separated by centrifugation of the microhematocrit tubes for 5 min at 12,000 rpm. The volumes of plasma, buffy coat and red blood cells were determined by measuring the microhematocrit tube using a ruler. Each fraction was then isolated and counted for their radioactivity in an automated gamma counter as described above. Data were expressed as percentage of injected dose (%ID), calculated as CPM in organ / total CPM recovered) × 100%, and SUV, calculated as (radioactivity in CPM in organ / weight of organ in g) / (total CPM recovered / total body weight in g). Data were presented using GraphPad Prism 10.0 software as mean ± SD, n = 3 per pre-treatment condition.

Statistical analysis

All statistical analysis was performed in GraphPad Prism 10.0 software. Significance was calculated using unpaired t-test (cell binding in LBT005, CME038 and NS/CT-2A cells) and ordinary one-way ANOVA with Dunnett's multiple comparisons tests (cell binding in MDA-MB-231 and U87 cells) or Tukey's multiple comparisons test (saturation in tissue homogenates). Two-way ANOVA and Šídák's (saturation in cells and biodistribution) or Dunnett's (TAC) multiple comparisons tests were employed for the analysis of the in vivo data. Significance is reported as follows: $P \leq 0.05$ (*), $P \leq 0.01$ (**), $P \leq 0.001$ (***), $P < 0.0001$ (****).

Results

IC_{50} assays

The IC_{50} value of various Hsp90 inhibitors were obtained in LBT005 and CME038 patient-derived glioblastoma lines and NS/CT-2A mouse neurospheres (Supplementary Fig. 1, Supplementary Table 2). HSP990 had sub-µM IC_{50} values across all cell lines and compared favourably to other inhibitors used, with most pronounced difference

observed in the NS/CT-2A neurospheres where it had outperformed other inhibitors except Ganetespib by at least 1–2 orders of magnitude.

[^{11}C]HSP990 cell binding

[^{11}C]HSP990 tracer binding was assessed in different Hsp90-expressing tumour cell lines, including MDA-MB-231 breast cancer, U87 glioblastoma, and LBT005, CME038 and NS/CT-2A glioma cells (Fig. 2A, Supplementary Table 3). Cellular tracer uptake was high in MDA-MB-231, U87, LBT005 and NS/CT-2A cells (4% act/10^5 cells), but lower (~1.5% act/10^5 cells) in the CME038 cells. Pre-incubation with HSP990 and structurally unrelated pan-Hsp90 inhibitors (Onalespib, PU-H71) reduced tracer binding (>85%, $P<0.0001$ for all except LBT005 and NS/CT-2A with $P\leq0.0003$), confirming saturable, Hsp90-specific binding in all tumour cell lines.

To explore the roles of Hsp90 isoforms in tracer binding in U87 and MDA-MB-231 cells, pre-incubation with isoform-selective inhibitors that have a markedly higher affinity towards certain Hsp90 isoforms over others was performed. Hsp90α-selective inhibitors (A1, A2) did not reduce cellular [^{11}C]HSP990 uptake. In contrast, Hsp90β-selective inhibitors (B1 and B2), particularly the more potent B2, reduced tracer binding by approximately 30–40% in both cell lines, while B1 showed a moderate reduction

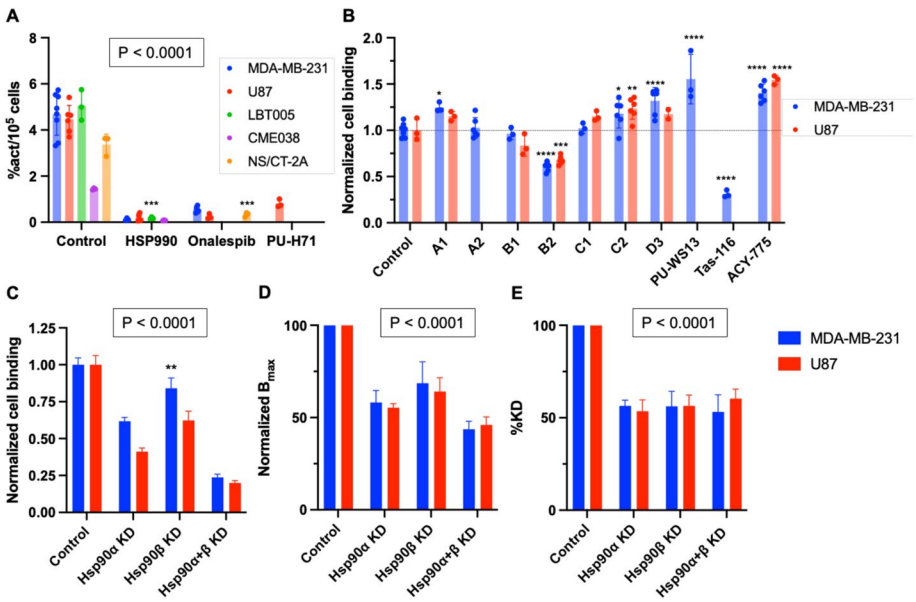

Fig. 2 In vitro cell binding. **A** MDA-MB-231, U87, LBT005, CME038 and NS/CT-2A cells were pre-incubated with vehicle (baseline) or 100 µM pan-selective Hsp90 inhibitors (block), followed by 250 kBq/mL [^{11}C]HSP990. Data are shown as %applied radioactivity bound to 1×10^5 cells **B** MDA-MB-231 and U87 cells were pre-incubated with 100 µM isoform-selective Hsp90 inhibitors (block): iHsp90α (A1, A2), iHsp90β (B1, B2), iGRP94 (C1, C2, PU-WS-13) and iTRAP1 (D3). Data are normalized to the baseline control conditions. Data in A-B are presented as mean ± SD, with individual values shown as dots **C** MDA-MB-231 and U87 cells were subjected to the DsiRNA-induced KD of Hsp90α, Hsp90β KD, or both isoforms 48 h before tracer incubation **D** B_{max} values were calculated from saturation binding curves obtained by incubating MDA-MB-231 and U87 Hsp90 KD cells with increasing concentrations of [^{3}H]HSP990 **E** Hsp90α/β protein levels following DsiRNA KD were determined by WB and expressed as %KD. Data in **C–E** are normalized to the negative control and presented as mean ± SD; statistics: $P\leq0.05$ (*), $P\leq0.01$ (**), $P\leq0.001$ (***), $P<0.0001$ (****), in (**A**), (**C**), (**D**), (**E**), $P<0.0001$ for all treatments compared to control, unless otherwise specified

(< 20%) in U87 but not MDA-MB-231 cells. The Hsp90α/β-selective inhibitor TAS-116 reduced binding by ~ 70% in MDA-MB-231 cells. Interestingly, GRP94-selective inhibitors (C1, C2 and PU-WS-13) and TRAP1-selective inhibitors (D3) increased tracer binding. HDAC6 inhibition with ACY-775 also significantly increased [^{11}C]HSP990 binding in MDA-MB-231 and U87 cells (Fig. 2B).

DsiRNA KD of Hsp90α, Hsp90β, or both isoforms significantly reduced [^{11}C]HSP990 tracer binding in U87 and MDA-MB-231 cell lines consistent with reduced protein expression levels observed by WB, which indicated binding specificity of the tracer to the cytosolic Hsp90 isoforms (Fig. 2C, E, Supplementary Table 4).

[^{3}H]HSP990 saturation binding

In vitro saturation binding assays with [^{3}H]HSP990 in U87 and MDA-MB-231 cells confirmed low nanomolar K_d values for both cell lines (Table 1, Supplementary Fig. 2). B_{max} values were nearly identical across two cell lines, and significantly reduced upon KD (30–60%), consistent with decreased Hsp90α and Hsp90β expression and with [^{11}C]HSP990 cell binding results (Fig. 2D, E, Supplementary Table 4).

Saturation binding was also performed on MDA-MB-231 and U87 tumour tissue homogenates and murine muscle and brain tissues (Table 1, Supplementary Fig. 2). Despite similar [^{11}C]HSP990 tracer uptake and B_{max} values for U87 and MDA-MB-231 cells, B_{max} was significantly lower in MDA-MB-231 tumour tissue compared to U87 tumour tissue. Muscle tissue showed significantly lower B_{max} values compared to tumour tissues, while the highest B_{max} value was observed in brain tissue. For all tissue homogenate samples, the observed B_{max} values were considerably lower than Hsp90α/β protein expression levels quantified by WB (Supplementary Table 5, Supplementary Fig. 3).

[^{11}C]HSP990 autoradiography

In vitro autoradiography was conducted on various tumour tissues and healthy murine muscle (Fig. 3). Tracer binding to sections of mouse B16.F10 melanoma, PC3 prostate carcinoma, NS/CT-2A glioma and U87 glioblastoma was high, significantly exceeding binding to healthy muscle tissue. This binding was Hsp90-specific, as pre-incubation with pan-selective Hsp90 inhibitors (HSP990, Onalespib, PU-H71) reduced tracer binding by over 85%. Pre-incubation with SNX-0723 yielded slightly lower blocking percentages of 60–70% for all tumour sections.

Table 1 In vitro [^{3}H]HSP990 saturation binding in U87 and MDA-MB-231 Hsp90 KD cells, and in MDA-MB-231 and U87 tumour, muscle and brain tissue homogenate samples. Calculated B_{max} (pmol/10^5 cells or pmol/mg protein or %of total protein) and K_d (nM) values are presented as mean ± SD

Tissue	Cells		Homogenates		
	B_{max}(pmol/10^5 cells)	K_d(nM)	B_{max}(pmol/mg)	B_{max}(%)	K_d(nM)
U87	3.9 ± 0.4	11 ± 3	56 ± 2	0.5 ± 0.02	2.2 ± 0.6
MDA-MB-231	3.9 ± 0.6	9 ± 1.9	19 ± 6	0.2 ± 0.05	1.3 ± 0.16
Muscle	–	–	4.9 ± 1.6	0.04 ± 0.014	1.2 ± 1.1
Brain	–	–	68 ± 2.1	0.6 ± 0.019	0.8 ± 0.09

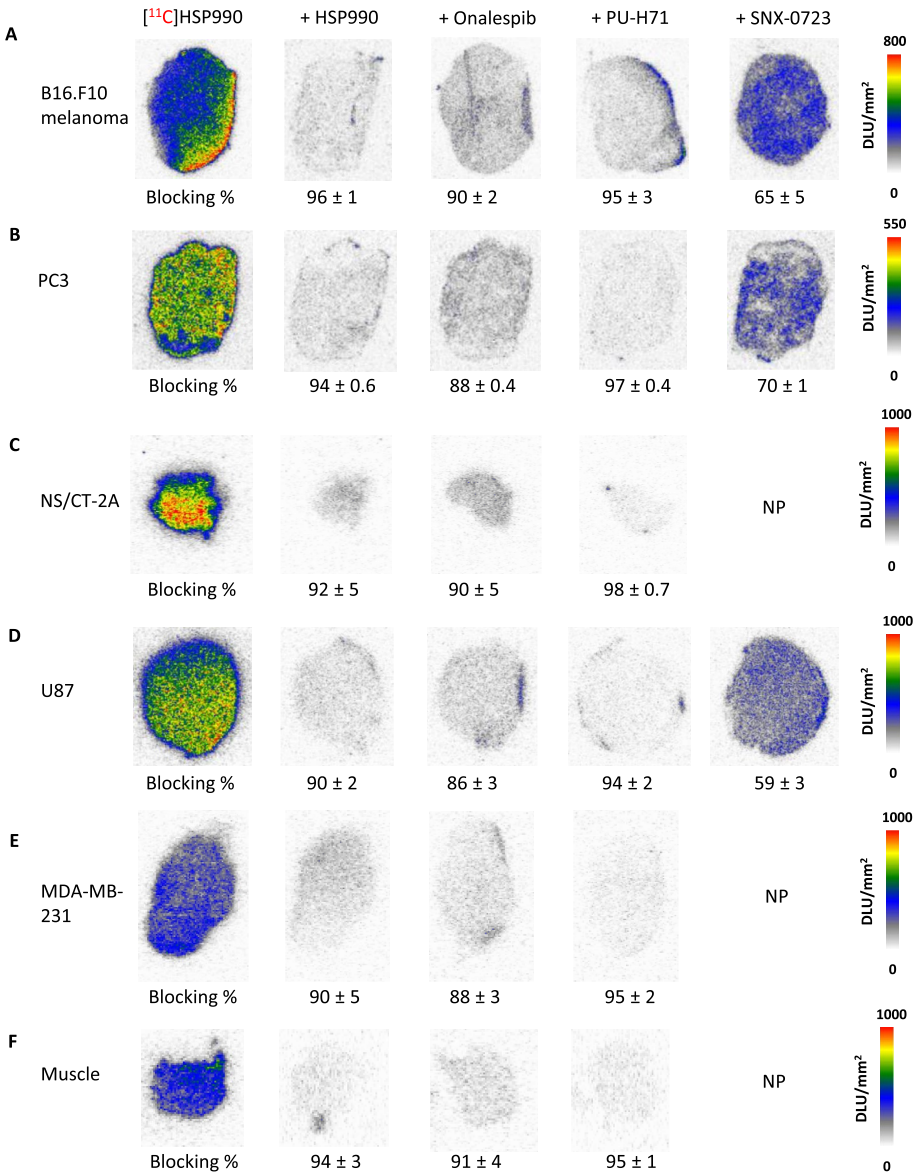

Fig. 3 In vitro [^{11}C]HSP990 autoradiography. Sections were pre-incubated with vehicle (baseline) or 10 µM Hsp90 inhibitors (block) followed by 74 kBq/mL [^{11}C]HSP990 **A** B16.F10 melanoma, **B** PC3 prostate tumour, **C** NS/CT-2A glioma, **D** U87 glioblastoma, **E** MDA-MB-231breast tumour and **F** muscle tissues. Intensity is expressed as DLU/mm^2; data are shown as mean ± SD, NP = not performed

Consistent with saturation binding assays on tissue homogenates, autoradiography revealed markedly lower tracer binding to MDA-MB-231 tumour sections compared to other tumour types, despite high specific cell binding to U87, MDA-MB-231, and NS/CT-2A tumour cells. Fluorescent staining with Hsp90 isoform-specific antibodies to tissue sections showed similar Hsp90α and Hsp90β expression levels (Supplementary Fig. 4).

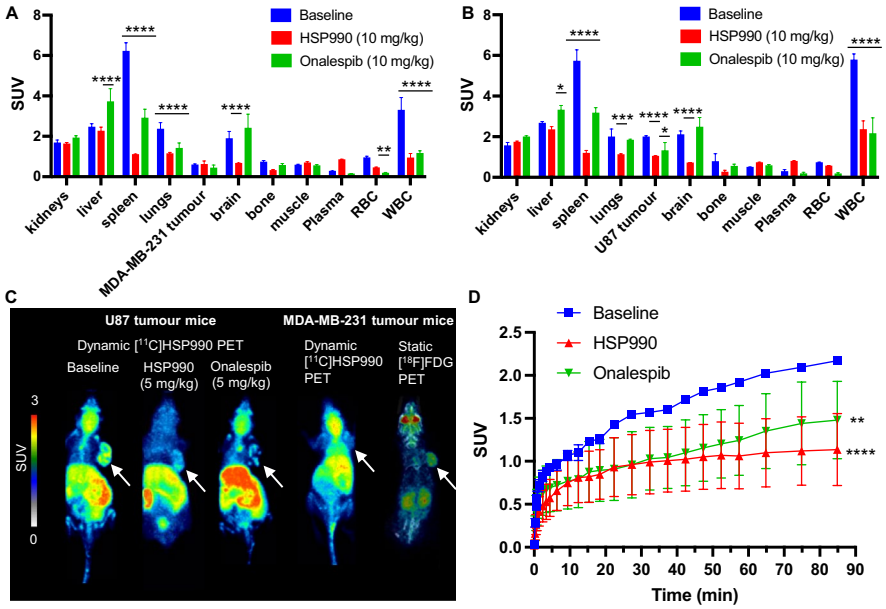

Fig. 4 [^{11}C]HSP990 biodistribution in subcutaneous MDA-MB-231 and U87 tumour xenograft mice. Ex vivo [^{11}C]HSP990 biodistribution in **A** MDA-MB-231 and **B** U87 tumour mice 60 min post-injection; mice were pre-treated with vehicle (baseline), or 10 mg/kg Hsp90 inhibitors (block) *i.p.* 60 min before [^{11}C]HSP990 injection, RBC and WBC stand to the red blood cells and white blood cells, respectively **C** In vivo [^{11}C]HSP990 µPET in U87 and MDA-MB-231 tumour mice; animals were pre-treated with vehicle (baseline), or 5 mg/kg Hsp90 inhibitors (block) *i.p.* 60 min before [^{11}C]HSP990 injection. Whole-body MIP of 15–90-min averaged dynamic [^{11}C]HSP990 and whole-body image of static 10 min [.^{18}F]FDG scans 60 min *p.i.* are shown. White arrows indicate tumour location **D** Corresponding averaged tumour SUV TACs of U87 tumour mice. Data are shown as mean ± SD; significance is reported for block vs baseline condition, $P \leq 0.05$ (*), $P \leq 0.01$ (**), $P \leq 0.001$ (***), $P < 0.0001$ (****)

[^{11}C]HSP990 biodistribution in subcutaneous immunocompromised tumour xenograft models

[^{11}C]HSP990 biodistribution was assessed in healthy mice and in subcutaneous MDA-MB-231 and U87 tumour xenograft models (Fig. 4A–B; Supplementary Table 6). Ex vivo biodistribution at 60 min *p.i.* revealed nearly identical tracer distribution across organs, except the tumour, in both healthy and tumour-bearing mice. High tracer accumulation was observed in the brain, white blood cells, and blood-rich organs (spleen and lungs) in all animals. Tracer binding in these organs was saturable and Hsp90-specific, as pre-treatment with HSP990 or Onalespib (10 mg/kg) significantly reduced tracer accumulation. Onalespib did not affect brain uptake due to its inability to cross the blood–brain-barrier.

Both HSP990 and Onalespib pre-treatment saturated Hsp90 binding in blood cells, reducing blood cell SUVs. For HSP990, this resulted in redistribution of [^{11}C]HSP990 from blood cells to plasma, increasing plasma SUV and tracer delivery to other organs. However, Onalespib did not increase plasma tracer concentration but instead shifted radioactivity from blood to the hepatobiliary system. This suggests that HSP990 pre-treatment partially blocks hepatobiliary clearance, while Onalespib pre-treatment facilitates faster hepatobiliary plasma clearance.

Ex vivo biodistribution and in vivo PET/CT imaging (Fig. 4A–D) demonstrated sustained [^{11}C]HSP990 uptake in U87 tumours. Tracer binding was saturable and Hsp90-specific, as evidenced by a significantly reduced uptake following pre-treatment with HSP990 or Onalespib (10 mg/kg) in ex vivo biodistribution experiment, as well by comparison of maximum intensity projection (MIP) images and time-activity curves (TACs) obtained by PET/CT following pre-treatment with HSP990 or Onalespib (5 mg/kg) *versus* baseline. In contrast, consistent with in vitro autoradiography and tumour homogenate saturation binding results, [^{11}C]HSP990 uptake was limited in MDA-MB-231 tumours at both imaging time points (4–5- and 7–8-weeks post-inoculation). However, high and homogeneous [^{18}F]FDG uptake in MDA-MB-231 tumours suggested metabolically active tumours with limited necrosis.

In vivo [^{11}C]HSP990 biodistribution in orthotopic immune competent syngeneic glioma model

Tracer biodistribution was assessed in NS/CT-2A neurosphere-derived high-grade glioma mouse model (Fig. 5 A-C, Supplementary Table 7). In vivo PET/CT imaging demonstrated high and saturable tracer accumulation in the brain of glioma-bearing mice, which decreased after pretreatment with HSP990 (5 mg/kg). However, no difference in tracer uptake was observed between the tumour-inoculated (right) and contralateral (left) brain hemispheres, as seen in µPET images and TACs. Ex vivo biodistribution at 60 min *p.i.* confirmed similar Hsp90-specific uptake in both hemispheres. Tracer biodistribution in other organs was similar to healthy mice and subcutaneous tumour models. The presence of the NS/CT-2A tumour in the right cerebrum was confirmed by H&E staining, and the tumour showed visible expression of Hsp90 isoforms (Supplementary Fig. 4, Supplementary Fig. 5).

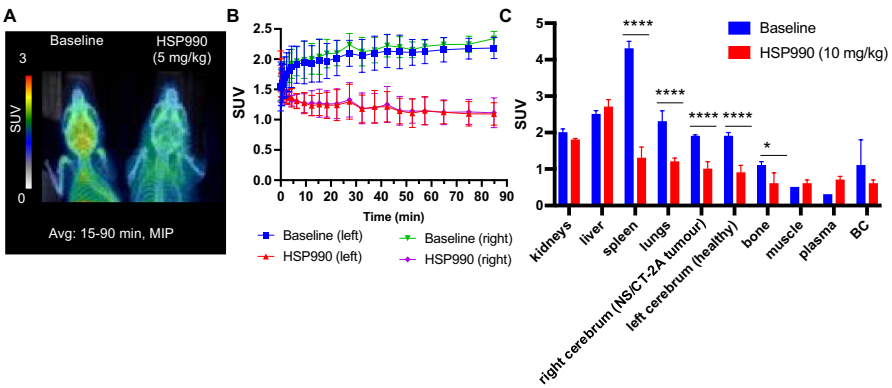

Fig. 5 [^{11}C]HSP990 biodistribution in orthotopic NS/CT-2A high grade glioma mice **A** In vivo [^{11}C]HSP990 µPET imaging studies; animals were pre-treated with vehicle (baseline), or 5 mg/kg HSP990 inhibitor (block) *i.p.* 60 min before [^{11}C]HSP990 injection; shown as whole-body MIP of 15–90-min averaged dynamic [^{11}C]HSP990 scans **B** Corresponding averaged brain SUV TACs. No significant difference between right (tumour) and left (healthy) cerebrums **C** Ex vivo [^{11}C]HSP990 biodistribution 60 min post-injection; mice were pre-treated with vehicle (baseline), or 10 mg/kg HSP990 inhibitor (block) *i.p.* 60 min before [^{11}C]HSP990 injection. Results are expressed as mean SUV ± SD. Significance is reported for block vs baseline condition, $P \leq 0.05$ (*), $P \leq 0.01$ (**), $P \leq 0.001$ (***), $P < 0.0001$ (****); no significant difference is observed right (tumour) and left (healthy) cerebrums

Discussion

Recently, we developed [^{11}C]HSP990 as an Hsp90-specific tracer for brain imaging and successfully translated the probe to the clinic. Here, we evaluated the utility of [^{11}C]HSP990 PET as a translational tool to study Hsp90 isoforms in tumours and support Hsp90-targeted therapeutic development. HSP990 is a promising Hsp90 inhibitor and has demonstrated selectivity for Hsp90 when tested against other kinases, as well as shown good oral bioavailability and blood–brain barrier permeability, making it a promising candidate for imaging brain malignancies (Menezes et al. 2012). HSP990, like most other small molecule Hsp90 inhibitors, targets the ATP-binding pocket of Hsp90. It is based on the aminopyrimidine scaffold structure with a nanomolar IC_{50} for Hsp90α, Hsp90β, and GRP94, and 320 nM for TRAP1. Hsp90 paralogues can display considerable differences in their amino acid sequences, explaining the variation in IC_{50}, however, the Hsp90 paralogues are highly conserved across species. For example, human and mouse Hsp90α display 99.9% sequence similarity.

[^{11}C]HSP990 displays Hsp90-specific binding to various cancer cell models in vitro

We found that [^{11}C]HSP990 binds specifically to Hsp90 in cultured breast tumour and glioma cell lines, as shown by blocking studies with structurally unrelated Hsp90 inhibitors, including the approved Hsp90 inhibitor TAS-116. This suggests that [^{11}C]HSP990 can be used to quantify tumour Hsp90 occupancy upon TAS-116 treatment and predict which patients may benefit from TAS-116 therapy. We investigated previously reported and investigational compounds with selectivity towards certain Hsp90 isoforms that have a markedly higher affinity for particular Hsp90 isoforms over others. Blocking with Hsp90β-selective inhibitor B2 reduced intracellular tracer binding, while inhibitors selective for other isoforms either did not reduce or even increased tracer binding. The increase in tracer uptake following the pre-incubation with some of the inhibitors such as C2 and D3 suggest the induction of the HSR by these inhibitors. HSR leads to the elevated levels of Hsp90 protein and therefore increased [^{11}C]HSP990 tracer uptake. Hsp90β-selective inhibitors, which have shown cytotoxicity without inducing the HSR, hold promise as therapeutic candidates, potentially circumventing the limitations associated with pan-Hsp90 inhibition (Mishra et al. 2021). The lack of blocking with other isoform-selective inhibitors can be explained by a much poorer affinity of these inhibitors compared to HSP990, with 100–1000-fold difference. Pre-incubation with the HDAC6 inhibitor ACY-775, which is known to enhance Hsp90 acetylation, increased tracer uptake, suggesting that HDAC6 inhibition enhances [^{11}C]HSP990 affinity for Hsp90, however, this requires further investigation (Backe et al. 2020). These findings support previous studies where HDAC inhibition lowered HSP990's IC_{50} in ovarian cancer cells, suggesting that combining HDAC and Hsp90 inhibitors enhances potency and synergy, and could improve therapeutic efficacy and enable lower dosing, thereby reducing side effects limiting the clinical application of Hsp90-targeting treatments (Moita et al. 2020). A similar sensitizing effect was reported in myeloma and anaplastic thyroid carcinoma cells using Luminespib as an Hsp90 inhibitor (Kim et al. 2015). Another possibility for increased uptake of [^{11}C]HSP990 is that HDAC6 inhibition leads to the hyperacetylation of Hsp90, leading to the disruption of Hsp90-client interactions including the release of

HSF1, which could lead to the activation of the HSR as with pan-Hsp90 inhibitors (Liu et al. 2021b).

Autoradiograms confirmed Hsp90-specific binding of [^{11}C]HSP990 to tumour tissue sections, with almost complete tracer binding reduction upon blocking with Hsp90 inhibitors. Slightly lower blocking percentages were observed with SNX-0723, possibly due to the slower kinetics and short incubation times. Tracer binding was lower in MDA-MB-231 tumour tissue compared to U87, which contrasts with in vitro cell binding results but aligns with the lower B_{max} values in tissue homogenates.

[^{3}H]HSP990 saturation binding reveals high affinity binding to cytosolic Hsp90 isoforms

In vitro saturation binding studies on wild type MDA-MB-231 and U87 cells and corresponding Hsp90 DsiRNA KD cells demonstrated specific binding to Hsp90α and Hsp90β isoforms, consistent with reported HSP990 affinity (Menezes et al. 2012). Saturation studies in MDA-MB-231 and U87 tumour tissue homogenates suggested tracer binding to a specific sub-pool of Hsp90α/β, as B_{max} values were ~ 9–18 times lower than Hsp90α/β protein expression levels determined by WB. This finding supports recent studies claiming the presence of the distinct "functionally active" and "latent" Hsp90 pools (Bhattacharya et al. 2022). In other studies, "active" Hsp90 has been defined as the druggable Hsp90 pool in cancer that has either a higher affinity for ATP or ATPase activity, or presence of specific Hsp90 post-translational modifications or incorporation into the multi-protein complexes termed epichaperomes (Barrott et al. 2013; Chakrabarty et al. 2024; Kamal et al. 2003). In our study, despite similar B_{max} values in cultured cells, the B_{max} value in MDA-MB-231 tumour tissue was significantly lower compared to U87, suggesting a distinct in vivo role for the "active" Hsp90 sub-pool across tumour types. Additionally, differential expression of Hsp90 across tissue types in vivo might be responsible for the observed results (Maiti and Picard 2022). In contrast to the previous studies with 17-*N*-allylamino-17-demethoxygeldanamycin (17-AAG), we saw no significant differences in affinity (K_d) between the tumour and healthy tissues. The higher observed affinity of 17-AAG to Hsp90 is most likely due to the drug's metabolism by NQO1/DT-diaphorase which produces a more potent 17-AAG hydroquinone, therefore previously reported increase in K_d must be interpreted with caution and studies should account for the differences in metabolic activity across cell types (Guo et al. 2005).

Differential expression of Hsp90 in vivo compared to in vitro might account for the differences in [^{11}C]HSP990 binding across tumour models

In vivo biodistribution studies of [^{11}C]HSP990 demonstrated high Hsp90-specific binding in the brain, white blood cells, blood-rich organs, and U87 tumour. Compared to our previous studies with [^{11}C]NMS-E973 and [^{11}C]YC-72-AB85, we did not observe higher tracer accumulation in blood cells of tumour-bearing mice when compared to the healthy controls, likely due to varying levels of Hsp90 shedding into the bloodstream across different tumour models (Vermeulen et al. 2021; Vermeulen et al. 2019; Zhang et al. 2017). Despite validation of the MDA-MB-231 tumour model using [^{18}F]FDG, no [^{11}C]HSP990 accumulation in the MDA-MB-231 tumours was observed in vivo, likely due to the low binding potential resulting from decreased B_{max} values, consistent with saturation binding studies. Both [^{11}C]HSP990 tracer uptake was lower in tissue

as well as immunofluorescent staining of tissue with Hsp90-specific mAbs was weaker in MDA-MB-231 cells compared to U87, in addition to the lower Hsp90 protein levels observed by WB in tissue homogenates. These data suggest differential Hsp90 expression in vitro *versus* in vivo across different tumour types. This result is similar to findings with the [^{18}F]PTP-Ganetespib tracer, where low in vivo tumour uptake was observed despite promising in vitro results (Kang et al. 2018). Similarly, an in vivo study using [^{124}I]PU-AD in an intracranial glioblastoma stem cell (GSC)-derived orthotopic patient-derived xenograft (PDX) tumour model also reported a heterogeneous tracer uptake. The study showed high and persistent uptake at 48 h post-injection in only a subset of GSC-derived glioblastoma tumours. Interestingly, high epichaperome levels in GSCs in culture correlated well with epichaperome-positive glioblastoma tumours in vivo. However, in one particular GSC type (GSC#8), a transition was observed from high epichaperome levels in vitro to epichaperome-negative tumours following transplantation. This molecular shift was confirmed using native gel electrophoresis, western blotting, and [^{131}I]PU-AD autoradiography (Bolaender et al. 2021b). These findings may suggest distinct Hsp90 states in vitro (cell culture) versus in vivo (xenograft), explaining the lack of translational efficacy observed in previous Hsp90 therapeutic studies. Moreover, these results imply that only certain tumour types may respond to Hsp90-targeting therapies, emphasizing the importance and potential of [^{11}C]HSP990 in patient stratification and monitoring therapeutic efficacy (Ginsberg et al. 2021). However, the hepatobiliary excretion of the tracer may limit its applicability for abdominal tumours and metastatic disease.

Limitations of [^{11}C]HSP990 tracer for cancer imaging

Despite a clear Hsp90-specific uptake of [^{11}C]HSP990 tracer in the U87 tumours in vivo, high non-specific tracer uptake in the abdominal organs such as liver as well as binding to blood cells limits the utility of the [^{11}C]HSP990 to the imaging of subcutaneous tumours where location of the lesion can be carefully controlled. Exploring orthotopic and metastatic Hsp90-expressing tumour models in small rodents might not be possible due to poor contrast in the abdomen, and a Hsp90 tracer with a better biodistribution might be needed to advance Hsp90 PET imaging in cancer.Blocking studies may impact both tracer binding to Hsp90 in blood cells and radiometabolism requiring determination of the plasma input curve for exact quantification of tumour uptake in blocked and control conditions.

High brain permeability of [^{11}C]HSP990 and strong tumour uptake in the subcutaneous U87 glioblastoma model prompted evaluation in a more comprehensive intracranial model that better reflects the aggressiveness of human glioblastoma. While [^{11}C]HSP990 demonstrated substantial Hsp90-specific uptake in NS/CT-2A brain tumours ex vivo, tracer uptake in vivo in tumours was similar to healthy brain tissue, providing insufficient tumour-to-background contrast. This outcome aligns with in vitro-derived B_{max}/K_d ratios from homogenate binding studies, which showed that tumour B_{max}/K_d values were not higher than healthy brain tissue. Consequently, these findings suggest that [^{11}C]HSP990 is not suitable for distinguishing glioma from healthy brain tissue in vivo but can still be used to visualize Hsp90 expression in glioma and quantify in vivo occupancy of Hsp90-targeting therapeutics. Especially in the context of brain malignancies,

this is extremely relevant for determining dosing strategies, as BBB permeability is often overestimated, as was the case with Onalespib (Canella et al. 2017).

Conclusion

[^{11}C]HSP990 is a suitable tracer for the identification of Hsp90-overexpressing tumours with confirmed specific binding both in vitro and in vivo. High [^{11}C]HSP990 tracer binding was observed in U87 glioblastoma xenografts and can be used to identify Hsp90 expression and quantify in vivo Hsp90 occupancy of therapeutics. Careful evaluation of Hsp90 protein levels in tissue of different tumour types followed by the [^{11}C]HSP990 in vivo evaluation in these models would shed more light on the applicability of this tracer to distinguish between high and low Hsp90-expressing tumours. For glioblastoma application in the intracranial model, [^{11}C]HSP990 image contrast in healthy brain *versus* NS/CT-2A tumour was insufficient to allow tumour delineation. Intracranial models using patient-derived glioblastoma or other human-derived glioblastoma cells can be investigated to compare with the NS/CT-2A mouse tumour model. Additionally, a clinical study in the glioblastoma patients to evaluate whether Hsp90 levels can be quantitatively assessed would shed more light on the potential of [^{11}C]HSP990 use for patient stratification and dose-occupancy studies in the context of Hsp90-targeted therapies. Developing a tracer with a longer half-life could be beneficial for investigating a time point at which tumour uptake might be higher than brain uptake, and one such tracer has already been attempted albeit with unsatisfactory results (Cools et al. 2025a).

Abbreviations

%ID	Percentage injected dose
17-AAG	17-*N*-Allylamino-17-demethoxygeldanamycin
ADP	Adenosine diphosphate
ATCC	American type culture collection
ATP	Adenosine triphosphate
BBB	Blood-brain barrier
B_{max}	Maximum binding capacity
CPM	Counts per minute
DLU/mm^2	Digital light units per square mm
DMEM	Dulbecco's Modified Eagle's Medium
DMF	Dimethylformamide
DMSO	Dimethylsulfoxide
FBS	Fetal bovine serum
GRP94	94 KDa glucose-regulated protein
GSAO	4-(N-(S-glutathionylacetyl)amino)phenylarsonous acid
HPLC	High-performance liquid chromatography
HSF1	Heat shock factor 1
Hsp90	Heat shock protein 90
HSR	Heat shock response
i.p.	Intraperitoneally
i.v.	Intravenously
IC_{50}	Half maximal inhibitory concentration
IRES	Internal ribosome entry site
K_d	Dissociation constant
KD	Knockdown
K_i	Inhibition constant
KO	Knockout
LC-MS	Liquid chromatography-mass spectrometry
MIP	Maximum intensity projection
MW	Molecular weight
NMR	Nuclear magnetic resonance
NP	Not performed
NSB	Non-specific binding
NTD	N-terminal domain
p.i.	Post-injection

PEI	Polyethylenimine
PET	Positron emission tomography
QC	Quality control
SD	Standard deviation
SUV	Standardized uptake value
TACs	Time-activity curves
TRAP1	Tumor necrosis factor receptor-associated protein 1
Tris HCl	Tris(hydroxymethyl)aminomethane hydrochloride
VOI	Volume of interest
WB	Western blot

Supplementary Information

The online version contains supplementary material available at https://doi.org/10.1186/s41181-025-00386-z.

Additional file1 (DOCX 6076 KB)

Acknowledgements
This work was supported by FWO (G0A6222N), VIB (C0401) and KU Leuven C2 (C24E/19/070). Financial support was also provided by the National Institutes of Health (CA270147 and DA052340). The PET-CT equipment was funded via an FWO medium infrastructure grant (AKUL15-30/G0H1216N). The authors gratefully acknowledge the VIB BioImaging Core Leuven for the microscopy support, namely the training and access to the Zeiss AxioScan.Z1 instrument; Becky Provinciael and Prof. Kurt Vermeire (Research Group of Molecular, Structural and Translational Virology, Rega Institute) for access to the tritium facilities and technical assistance; and Julie Cornelis (Laboratory for Radiopharmaceutical Research, KU Leuven) for the realization of in vivo and ex vivo studies.

Author contributions
GB is responsible for the study conception and design. Experimental investigation, methodology and formal analysis were performed by RC, VN, SJM, MD, AZZ, and MR. GB, FR, JS, KV, BSJB, FDS, AC are responsible for funding acquisition, and/or resources and/or supervision. The first draft of the manuscript was written by RC and VN who are also responsible for data visualization; all authors reviewed draft versions of the manuscript. All authors read and approved the final manuscript.

Funding
This work was supported by FWO (G0A6222N), VIB (C0401) and KU Leuven C2 (C24E/19/070). Financial support also provided by the National Institutes of Health (CA270147 and DA052340). The PET-CT equipment was funded via an FWO medium infrastructure grant (AKUL15-30/G0H1216N).

Data availability
The datasets generated during and/or analysed during the current study are available from the corresponding author on reasonable request.

Declarations

Ethics approval and consent to participate
This study was performed in line with the principles of the Declaration of Helsinki. Approval was granted by the local Ethics Committee for Animals and use of patient-derived cell lines (P190-2019, P169-2024, S69409) and carried out in accordance with the ARRIVE guidelines.

Consent for publication
Not applicable.

Competing interest
The authors have no relevant financial or non-financial interests to disclose.

Author details
[1]Present Address: Laboratory for Radiopharmaceutical Research, Department of Pharmaceutical and Pharmacological Sciences, KU Leuven, 3000 Louvain, Belgium. [2]Switch Laboratory, VIB Center for Brain and Disease Research, Herestraat 49, 3000 Louvain, Belgium. [3]Present Address: Switch Laboratory, Department of Cellular and Molecular Medicine, KU Leuven, Herestraat 49, 3000 Louvain, Belgium. [4]NURA, Belgian Nuclear Research Centre (SCK CEN), 2400 Mol, Belgium. [5]Warren Family Research Center for Drug Discovery and Development and Department of Chemistry & Biochemistry, University of Notre Dame, 305 McCourtney Hall, Notre Dame, IN 46556, USA. [6]Department of Medicinal Chemistry, The University of Kansas, 1251 Wescoe Hall Drive, Malott Hall 4070, Lawrence, KS 66045, USA. [7]The Laboratory for Precision Cancer Medicine, Translational Cell and Tissue Research Unit, Department of Imaging & Pathology, KU Leuven, 3000 Louvain, Belgium. [8]The KU Leuven Institute for Single-Cell Omics (LISCO), KU Leuven, Louvain, Belgium. [9]The Leuven Cancer Institute (LKI), KU Leuven, Louvain, Belgium. [10]Laboratory for Tumour Immunology and Immunotherapy, Department Oncology, 3000 Leuven, KU Leuven, Belgium. [11]Department of Neurosurgery, CHU UCL Namur Site Godinne, Université Catholique de Louvain, 5530 Yvoir, Belgium.

Received: 24 June 2025 Accepted: 7 September 2025
Published online: 26 September 2025

References

Babi A, Menlibayeva K, Bex T, Doskaliev A, Akshulakov S, Shevtsov M. Targeting heat shock proteins in malignant brain tumors: from basic research to clinical trials. Cancers. 2022;14(21):5435.
Backe SJ, Sager RA, Woodford MR, Makedon AM, Mollapour M. Post-translational modifications of Hsp90 and translating the chaperone code. J Biol Chem. 2020;295(32):11099–117.
Barrott JJ, Hughes PF, Osada T, Yang X-Y, Hartman ZC, Loiselle DR, et al. Optical and radioiodinated tethered Hsp90 inhibitors reveal selective internalization of ectopic Hsp90 in malignant breast tumor cells. Chem Biol. 2013;20(9):1187–97.
Bhattacharya K, Maiti S, Zahoran S, Weidenauer L, Hany D, Wider D, et al. Translational reprogramming in response to accumulating stressors ensures critical threshold levels of Hsp90 for mammalian life. Nat Commun. 2022;13(1):6271.
Bolaender A, Zatorska D, He H, Joshi S, Sharma S, Digwal CS, et al. Chemical tools for epichaperome-mediated interactome dysfunctions of the central nervous system. Nat Commun. 2021a;12(1):4669.
Burns HD, Van Laere K, Sanabria-Bohórquez S, Hamill TG, Bormans G, Eng W, et al. [18 F]MK-9470, a positron emission tomography (PET) tracer for in vivo human PET brain imaging of the cannabinoid-1 receptor. Proc Natl Acad Sci. 2007;104(23):9800–5. https://doi.org/10.1073/pnas.0703472104.
Canella A, Welker AM, Yoo JY, Xu J, Abas FS, Kesanakurti D, et al. Efficacy of Onalespib, a long-acting second-generation HSP90 inhibitor, as a single agent and in combination with temozolomide against malignant gliomas. Clin Cancer Res. 2017;23(20):6215–26.
Chakrabarty S, Wang S, Roychowdhury T, Ginsberg SD, Chiosis G. Introducing dysfunctional protein-protein interactome (dfPPI)—A platform for systems-level protein-protein interaction (PPI) dysfunction investigation in disease. Curr Opin Struct Biol. 2024;1(88):102886.
Cools R, Vermeulen K, Celen S, Leitao RCF, Bormans G. Radiosynthesis and evaluation of [18 F]FEHSP990 as novel PET tracer for Hsp90 PET imaging. J Label Comp Radiopharm. 2025a;68(4):e4144. https://doi.org/10.1002/jlcr.4144.
Cools R, Vermeulen K, Narykina V, Leitao RCF, Bormans G. Radiosynthesis and preclinical evaluation of [11C]SNX-ab as an Hsp90α, β isoform-selective PET probe for in vivo brain and tumour imaging. EJNMMI Radiopharm Chem. 2023;8(1):2. https://doi.org/10.1186/s41181-023-00189-0.
Cools R, Vermeulen K, Vonck E, Baekelandt V, Varlow C, Narykina V, et al. In vivo visualization and quantification of brain heat shock protein 90 with [11 C]HSP990 in healthy aging and neurodegeneration. J Nucl Med. 2025b;124:268961. https://doi.org/10.2967/jnumed.124.268961.
Csermely P, Schnaider T, Soti C, Prohászka Z, Nardai G. The 90-kDa molecular chaperone family: structure, function, and clinical applications. A comprehensive review. Pharmacol Ther. 1998;79(2):129–68.
Dunphy MPS, Pressl C, Pillarsetty N, Grkovski M, Modi S, Jhaveri K, et al. First-in-human trial of epichaperome-targeted PET in patients with cancer. Clin Cancer Res. 2020;26(19):5178–87.
Ginsberg SD, Joshi S, Sharma S, Guzman G, Wang T, Arancio O, et al. The penalty of stress—Epichaperomes negatively reshaping the brain in neurodegenerative disorders. J Neurochem. 2021;159(6):958–79.
Grad I, Cederroth CR, Walicki J, Grey C, Barluenga S, Winssinger N, et al. The Molecular chaperone Hsp90α is required for meiotic progression of spermatocytes beyond pachytene in the mouse. PLoS ONE. 2010;5(12):e15770. https://doi.org/10.1371/journal.pone.0015770.
Guo W, Reigan P, Siegel D, Zirrolli J, Gustafson D, Ross D. Formation of 17-allylamino-demethoxygeldanamycin (17-AAG) hydroquinone by NAD(P)H:quinone oxidoreductase 1: role of 17-AAG hydroquinone in heat shock protein 90 inhibition. Cancer Res. 2005. https://doi.org/10.1158/0008-5472.CAN-05-2029.
Ho Shon I, Kumar D, Sathiakumar C, Berghofer P, Van K, Chicco A, et al. Biodistribution and imaging of an hsp90 ligand labelled with 111In and 67Ga for imaging of cell death. EJNMMI Res. 2020;10(1):4. https://doi.org/10.1186/s13550-020-0590-x.
Horti AG, Fan H, Kuwabara H, Hilton J, Ravert HT, Holt DP, et al. 11C-JHU75528: a radiotracer for PET imaging of CB1 cannabinoid receptors. J Nucl Med. 2006;47(10):1689–96.
Huang KH, Veal JM, Fadden RP, Rice JW, Eaves J, Strachan JP, et al. Discovery of novel 2-aminobenzamide inhibitors of heat shock protein 90 as potent, selective and orally active antitumor agents. J Med Chem. 2009;52(14):4288–305.
Kamal A, Thao L, Sensintaffar J, Zhang L, Boehm MF, Fritz LC, et al. A high-affinity conformation of Hsp90 confers tumour selectivity on Hsp90 inhibitors. Nature. 2003;425(6956):407–10.
Kang J, Young Lee J, Taş İ, More KN, Kim H, Park J-H, et al. Radiosynthesis, biological evaluation and preliminary microPET study of 18F-labeled 5-resorcinolic triazolone derivative based on ganetespib targeting HSP90. Bioorg Med Chem Lett. 2018;28(23–24):3658–64.
Kim SH, Kang JG, Kim CS, Ihm S-H, Choi MG, Yoo HJ, et al. Novel heat shock protein 90 Inhibitor NVP-AUY922 synergizes with the histone deacetylase inhibitor PXD101 in induction of death of anaplastic thyroid carcinoma cells. J Clin Endocrinol Metab. 2015;100(2):E253–61. https://doi.org/10.1210/jc.2014-3101.
Kurokawa Y, Honma Y, Sawaki A, Naito Y, Iwagami S, Komatsu Y, et al. Pimitespib in patients with advanced gastrointestinal stromal tumor (CHAPTER-GIST-301): a randomized, double-blind, placebo-controlled phase III trial. Ann Oncol. 2022;33(9):959–67.
Li F, Fan Y, Zhou L, Martin DR, Liu Z, Li Z. Synthesis and characterization of 64Cu-labeled Geldanamycin derivative for imaging HSP90 expression in breast cancer. Nucl Med Biol. 2024;136–137:108929.
Liu H, Zhang Z, Huang Y, Wei W, Ning S, Li J, et al. Plasma HSP90AA1 predicts the risk of breast cancer onset and distant metastasis. Front Cell Dev Biol. 2021a;24:9. https://doi.org/10.3389/fcell.2021.639596/full.
Liu P, Xiao J, Wang Y, Song X, Huang L, Ren Z, et al. Posttranslational modification and beyond: interplay between histone deacetylase 6 and heat-shock protein 90. Mole Med. 2021b;27(1):110. https://doi.org/10.1186/s10020-021-00375-3.
Maiti S, Picard D. Cytosolic Hsp90 Isoform-specific functions and clinical significance. Biomolecule. 2022;12(9):1166.

Menezes DL, Taverna P, Jensen MR, Abrams T, Stuart D, Yu GK, et al. The novel oral Hsp90 inhibitor NVP-HSP990 exhibits potent and broad-spectrum antitumor activities In Vitro and In Vivo. Mol Cancer Ther. 2012;11(3):730–9.
Mishra SJ, Liu W, Beebe K, Banerjee M, Kent CN, Munthali V, et al. The development of Hsp90β-selective inhibitors to overcome detriments associated with pan-Hsp90 inhibition. J Med Chem. 2021;64(3):1545–57.
Moita AJR, Bandolik JJ, Hansen FK, Kurz T, Hamacher A, Kassack MU. Priming with HDAC inhibitors sensitizes ovarian cancer cells to treatment with cisplatin and HSP90 inhibitors. Int J Mol Sci. 2020;21(21):1–22.
Monazzam A, Razifar P, Ide S, Rugaard Jensen M, Josephsson R, Blomqvist C, et al. Evaluation of the Hsp90 inhibitor NVP-AUY922 in multicellular tumour spheroids with respect to effects on growth and PET tracer uptake. Nucl Med Biol. 2009;36(3):335–42.
Nam HY, Lee HW. Relationship between 18F-FDG uptake and heat shock protein 90α expression in colorectal cancer. Hell J Nucl Med. 2021;24(1):10–7.
Narykina V, Kleynhans J, Cawthorne C, Schymkowitz J, Rousseau F, Bormans G. Development and evaluation of Hsp90-targeting nanobodies for visualisation of extracellular Hsp90 in tumours using PET imaging. EJNMMI Radiopharm Chem. 2025;10(1):10. https://doi.org/10.1186/s41181-025-00331-0.
Nordeman P, Jayendra ZP, Briard E, Li SC, Larhed M, Antoni G, et al. 18F-radiolabeling and preliminary evaluation of a HSP90 ligand. Eur J Pharm Sci. 2021;157:105647.
Orth M, Albrecht V, Seidl K, Kinzel L, Unger K, Hess J, et al. Inhibition of HSP90 as a strategy to radiosensitize glioblastoma: targeting the DNA damage response and beyond. Front Oncol. 2021;11:612354. https://doi.org/10.3389/fonc.2021.612354/full.
Oude Munnink TH, de Korte MA, Nagengast WB, Timmer-Bosscha H, Schröder CP, de Jong JR, et al. 89Zr-trastuzumab PET visualises HER2 downregulation by the HSP90 inhibitor NVP-AUY922 in a human tumour xenograft. Eur J Cancer. 2010;46(3):678–84.
Park D, Don AS, Massamiri T, Karwa A, Warner B, MacDonald J, et al. Noninvasive imaging of cell death using an Hsp90 ligand. J Am Chem Soc. 2011;133(9):2832–5. https://doi.org/10.1021/ja110226.
Pool M, Terwisscha van Scheltinga AGT, Kol A, Giesen D, de Vries EGE. Lub-de Hooge MN. 89Zr-Onartuzumab PET imaging of c-MET receptor dynamics. Eur J Nucl Med Mol Imaging. 2017;44(8):1328–36. https://doi.org/10.1007/s00259-017-3672-x.
Rastogi S, Joshi A, Sato N, Lee S, Lee M-J, Trepel JB, et al. An update on the status of HSP90 inhibitors in cancer clinical trials. Cell Stress Chaperones. 2024;29(4):519–39.
Riva M, Wouters R, Weerasekera A, Belderbos S, Nittner D, Thal DR, et al. CT-2A neurospheres-derived high-grade glioma in mice: a new model to address tumor stem cells and immunosuppression. Biol Open. 2019;8(9):044552. https://doi.org/10.1242/bio.044552/266050/CT-2A-neurospheres-derived-high-grade-glioma-in.
Sakai T, Ogata A, Ikenuma H, Yamada T, Hattori S, Abe J, et al. A novel PET probe to selectively image heat shock protein 90α/β isoforms in the brain. EJNMMI Radiopharm Chem. 2024;9(1):19. https://doi.org/10.1186/s41181-024-00248-0.
Sartori E, Langer R, Vassella E, Hewer E, Schucht P, Zlobec I, et al. Low co-expression of epidermal growth factor receptor and its chaperone heat shock protein 90 is associated with worse prognosis in primary glioblastoma, IDH-wild-type. Oncol Rep. 2017;38(4):2394–400. https://doi.org/10.3892/or.2017.5863.
Seyfried TN, El-Abbadi M, Roy ML. Ganglioside distribution in murine neural tumors. Mol Chem Neuropathol. 1992. https://doi.org/10.1007/BF03159989.
Smith-Jones PM, Solit D, Afroze F, Rosen N, Larson SM. Early tumor response to Hsp90 therapy using HER2 PET: comparison with 18F-FDG PET. J Nucl Med. 2006;47(5):793–6.
Vermeulen K, Cools R, Briard E, Auberson Y, Schoepfer J, Koole M, et al. Preclinical evaluation of [11 C]YC-72-AB85 for In Vivo visualization of heat shock protein 90 in brain and cancer with positron emission tomography. ACS Chem Neurosci. 2021;12(20):3915–27. https://doi.org/10.1021/acschemneuro.1c00508.
Vermeulen K, Naus E, Ahamed M, Attili B, Siemons M, Luyten K, et al. Evaluation of [11 C]NMS-E973 as a PET tracer for in vivo visualisation of HSP90. Theranostics. 2019;9(2):554–72.
Voss AK, Thomas T, Gruss P. Mice lacking HSP90β fail to develop a placental labyrinth. Development. 2000;127(1):1–11.
Wang X, Han Z, Zhang J, Chen M, Meng W. Development and preclinical evaluation of ^{18} F-Labeled PEGylated sansalvamide A decapeptide for noninvasive evaluation of Hsp90 status in pancreas cancer. Mol Pharm. 2024;21(10):5238–46. https://doi.org/10.1021/acs.molpharmaceut.4c00643.
Wang X, Zhang J, Han Z, Ma L, Li Y. ^{18} F-labeled dimer-sansalvamide a cyclodecapeptide: a novel diagnostic probe to discriminate pancreatic cancer from inflammation in a nude mice model. J Cancer. 2022;13(6):1848–58.
Wang X, Zhang J, Wu H, Li Y, Conti PS, Chen K. PET imaging of Hsp90 expression in pancreatic cancer using a new 64Cu-labeled dimeric sansalvamide a decapeptide. Amino Acids. 2018;50(7):897–907. https://doi.org/10.1007/s00726-018-2566-y.
Zhang G, Liu Z, Ding H, Zhou Y, Doan HA, Sin KWT, et al. Tumor induces muscle wasting in mice through releasing extracellular Hsp70 and Hsp90. Nat Commun. 2017;8(1):589.

Publisher's Note